

A black and white photograph of a jet engine fan, showing the central hub and the curved blades radiating outwards. The image is used as a background for the text.

SEMINÁRIOS PPG-EM / UERJ 2021

PPG-EM UERJ 2021 SEMINARS

**Programa de Pós-graduação em Engenharia
Mecânica UERJ**

Graduate Program in Mechanical Engineering UERJ



SEMINÁRIOS PPG-EM / UERJ 2021

PPG-EM UERJ 2021 SEMINARS

**Programa de Pós-graduação em Engenharia
Mecânica UERJ**

Graduate Program in Mechanical Engineering UERJ



WWW.PPGEM.UERJ.BR

Editado por Prof. Daniel J. N. M. Chalhub.

Reprodução é permitida sem restrições. O layout foi criado a partir do modelo \LaTeX “The Legrand Orange Book”, versão 2.1 (14/11/2015), sob a licença Creative Commons:

CC BY-NC-SA 3.0 (<http://creativecommons.org/licenses/by-nc-sa/3.0/>)

Capa: “Rotor de motor-turbina de aeronave”. Créditos de imagem: Usuário blickpixed do Pixabay. <https://pixabay.com/photos/turbine-aircraft-motor-rotor-590354/>

Foto dos cabeçалhos: “Motor turbojato – Rolls-Royce”. Créditos de imagem: Usuário stux do Pixabay. <https://pixabay.com/photos/engine-turbo-jet-engine-rolls-royce-103079/>

Edited by Prof. Daniel J. N. M. Chalhub.

There are no restrictions for reproducing this material. The layout was created from the \LaTeX template “The Legrand Orange Book”, version 2.1 (14/11/15), under the Creative Commons license:

CC BY-NC-SA 3.0 (<http://creativecommons.org/licenses/by-nc-sa/3.0/>)

Cover: “Turbine aircraft motor rotor”. Image by Pixabay user blickpixed <https://pixabay.com/photos/turbine-aircraft-motor-rotor-590354/>

Header image: “Turbo jet engine – Rolls-Royce”. Image by Pixabay user stux <https://pixabay.com/photos/engine-turbo-jet-engine-rolls-royce-103079/>

May 20, 2022



Sumário / Contents

1 Mini-artigos / Short papers 9

February 23, 2021

- 1.1 **Bruno Campos dos Santos** 10
PUBLIC POLICIES TO INCENTIVE THE GENERATION OF PHOTOVOLTAIC ENERGY

May 11, 2021

- 1.2 **Marcos Paulo Dornellas** 12
POROSITY MEASUREMENT IN B4C-NB COMPOSITE THROUGH DIGITAL IMAGE ANALYSIS AND PROCESSING

May 18, 2021

- 1.3 **Rogério Pazetto Saldanha da Gama** 14
ON THE FICK'S SECOND LAW WITH CONCENTRATION-DEPENDENT DIFFUSION COEFFICIENT

July 06, 2021

- 1.4 **Carolina Sanchez Guerrero** 16
ASSESSMENT OF THE DYNAMIC RESPONSE AND FATIGUE ANALYSIS OF STEEL-CONCRETE COMPOSITE FLOORS

November 10, 2021

1.5	Adilson Claudio Quizunda	18
	<i>SYNTHESIS AND CHARACTERIZATION OF NANOSTRUCTURED HYDROXIAP-ATITE FOR APPLICATIONS AS CATALYST IN THE PRODUCTION OF BIOFUELS</i>	
1.6	Bruno Neves Targino Teodoro	20
	<i>EVALUATION OF THE APPLICATION OF A TIN FILM ON AISI 1045 STEEL TOOLS FOR THE FRICTION STIR WELDING PROCESS, FSW</i>	
1.7	Carolina Andrea Sanchez Guerrero	22
	<i>DYNAMIC ANALYSIS OF BUILDINGS CONSIDERING THE EFFECT OF MASONRY INFILLS</i>	
	November 17, 2021	
1.8	Jonatas Motta Quirino	24
	<i>NONLINEAR HEAT TRANSFER STUDY IN RADIAL POROUS FINS</i>	
	November 24, 2021	
1.9	Haroldo Rosman	26
	<i>NUMERICAL SIMULATION OF TRANSPORT THROUGH POLYMER LAYER AND POROUS ARTERIAL WALL OF SIROLIMUS AND PACLITAXEL IN DRUG-ELUTING STENTS</i>	
1.10	Uly Guimarães Rocha	28
	<i>SEALANT WITH SILVER ADDITIVE AND ITS EFFECTIVENESS IN COMBATING HOSPITAL BACTERIA</i>	
1.11	William Montijo de Oliveira	30
	<i>DETERMINATION OF THERMAL CONDUCTIVE OF POLYMERIC MATRIX NANOCOM-POSITES WITH GRAPHENE OXIDE CHARGES BY HOT PLARE METHOD</i>	



1. Mini-artigos / Short papers

20 de maio de 2022

Neste capítulo são apresentados os mini-artigos dos onze trabalhos científicos que fizeram parte dos Seminários do PPG-EM em 2021. Devido a pandemia de COVID-19, os Seminários do PPG-EM 2021 foram realizados em formato online. Os trabalhos estão organizados segundo a data de apresentação.

Prof. Daniel J. N. M. Chalhub, D.Sc.
Coordenador dos Seminários PPG-EM 2021

May 20, 2022

This chapter presents the short papers of the eleven scientific papers that participated in the PPG-EM Seminars in 2021. Due to the COVID-19 pandemic, the PPG-EM 2021 Seminars were held online. Papers are organized according to the date of presentation.

Prof. Daniel J. N. M. Chalhub, D.Sc.
PPG-EM 2021 Seminars Chair



PUBLIC POLICIES TO INCENTIVE THE GENERATION OF PHOTOVOLTAIC ENERGY

Author: Bruno Campos dos Santos¹ bruno.campos@ifrj.edu.br
Advisor(s): Manoel Antônio Da Fonseca Costa Filho¹

¹ Rio de Janeiro State University

PPG-EM Seminars: season 2021
<http://www.ppgem.uerj.br>

April 15, 2021

Keywords: Photovoltaic energy, Incentive mechanisms, Distributed generation, Solar energy.

1 Introduction

Currently, countries are faced with the indispensability to demonstrate their commitment to the environmental issue. This commitment added to the growing energy demand presents as a gateway to the insertion of new technologies and large-scale expansion of energy generation, production and distribution from renewable sources. The present manuscript aimed to indicate which mechanisms of incentive to the distributed generation of photovoltaic energy are more suitable for the Brazilian scenario [6].

2 Methods

The methodology used here is based, primarily, on identifying the countries with best practices in the area of production and distribution of renewable energy, specifically photovoltaics, and their incentive mechanisms (Benchmarking).

3 Benchmarking: Public policies to incentive the generation of photovoltaic energy.

This section provide an overview of the leading countries in photovoltaic energy production and also of the Brazilian scenario.

3.1 Leading countries in photovoltaic power generation.

It is generally agreed, a fact portrayed in several basic books on solar energy that the sun's energy is transmitted to our planet through space in the form of electromagnetic radiation. This radiation consists of electromagnetic waves with different frequencies and wavelengths. The higher the frequency, the greater the energy transmitted. The incident solar energy always generates heating, unless it is completely reflected.

In a similar way, it is well known that the world is experiencing an upward expansion in the capacity of generating energy with the use of renewable sources. There is also an increasing need to use clean energy sources to

protect the environment from the rampant use of fossil fuels that cause significant damage to diverse ecosystems around the world, in addition to contributing to the increase in global temperature.

This idea can be seen through the large share that renewable sources represent, on the enlargement of the capacity of energy generation installed in Europe, in 2017, being of the order of 85%, considering all existing technologies [2].

Among so many aspects that support this argument, necessary in this article, China, Japan and Germany deserve to be highlighted on the world stage, when considering a capacity to generate energy from renewable sources (excluding hydroelectric generation). These nations use one or more of the main mechanisms for promoting renewable sources: Feed-In Tariff (FIT), Net Metering, Auctions, Quotas with Certificates Trading and Rebate [3].

3.2 Incentive mechanisms for the insertion of photovoltaic energy in Brazil.

In Brazil, Net Metering is the most used incentive mechanism for the production of photovoltaic energy for distributed generation, which does not allow remuneration to the producer. And energy auctions are commonly used for centralized PV generation.

According to Costa Filho and Chiganer [7] (2013), in early 2013, the Solar Fund was created, which aimed to encourage the development of the photovoltaic market in Brazil, through a financial support consisting of a non-refundable resource, supporting the first connected projects to the network. Any individual or legal entity interested in installing a photovoltaic microgenerator with a power of up to 5 KWp connected to the network, integrated into a building and participating in the energy compensation system (as provided for in ANEEL Resolution 482/2012), may request support from the Solar Fund.

The Support Program for Energy Conservation Service Companies (PROESCO), whose line of action is support for efficiency projects, focusing on energy distribution and power management, is an effective measure to encourage the growth of photovoltaic energy generation.

4 Results

China uses two basic policies to promote renewable energies: Feed-In Tariff, with the intention of offering subsidies and guarantees to the renewable energy producer, and Energy Auctions with quotas, which guarantee that a portion of the auctioned energy will be used to build renewable power plants. This has a direct effect on the incentive to produce photovoltaic energy, using direct subsidies and specific quotas for the generation of solar energy [4].

Japan frequently adopts the Feed-in Tariff mechanism, combined with prizes for clean energy generation, according to the Agency for Natural Resources and Energy [5]. The Japanese government, through the Ministry of Economy, Trade and Industry (METI), implemented Feed-in Tariff in July 2012, replacing the Renewable Portfolio Standards (RPS) mechanism, and revising the standard used for the photovoltaic energy purchasing.

Germany uses renewable energy as promotion tools: Feed-in Tariff and Auctions with quotas for renewable energy. As a result, questions arise regarding the costs of implementing these renewable energy promotion policies, which lead to the wrong conclusion that support for these energies would be expensive to German government. For Pegels and Lutkenhorst [1], this affirmation does not match the reality of the facts, since the total cost of the subsidy for the Feed-in Tariff policy is not greater than the cost of the subsidy for electricity generated on a coal-fired or nuclear power plants.

The main national energy transition project (Energiewende), which prioritizes renewable energy sources, which was carried out in Germany, one of the most ambitious countries regarding the transition from non-renewable energy sources to renewable energy sources [1], is based on the Feed-in Tariff (FIT) mechanism acting as a central element of the policy package in Germany and then it has to be highlighted.

5 Conclusions

The Brazilian scenario outlined by continental proportions requires a sectorization in the use of renewable sources of energy according to the offer of the energy resource, we have as examples: wind, solar, biofuels and others.

And policies that encourage the production of these types of energy, should be based primarily on the models: Feed-in Tariff, Net Metering, Rebates and auctions with quotas for renewable energies, which provide greater security to the producer of clean energy, through fixed rates, in other words, fixed prices and a guaranteed purchase of energy for decades, a factor that inspires greater security in investment in the production and distribution of renewable energy.

References

- [1] PEGELS. A and LÜTKENHORST. W. Is germanys energy transition a case of successful green industrial policy? contrasting wind and solar pv. *Energy*

Policy, 74:S/N, 2014.

- [2] EEA (European Energy Agency). Renewable energy in europe — 2018; recent growth and knockon effects. Technical report, EEA, 2018.
- [3] DOS SANTOS. Bruno Campos, COSTA FILHO. M. A. F., and NICHIOKA. Júlio. Benchmarking: Políticas públicas de incentivo a geração de energia fotovoltaica. *Episteme Transversalis*, 10:S/N, 2019.
- [4] IEA (Agência Internacional de Energia). Countries non members. Technical report, IEA, 2017.
- [5] ANRE (Agency for Natural Resources and Energy). Status of renewable sources. Technical report, ANRE, 2017.
- [6] REN21 (Renewable Energy Policy Network for the 21st Century). Renewables global futures report: Great debates towards 100% renewable energy. Technical report, REN21, 2017.
- [7] COSTA FILHO. M. A. F. and CHIGANER, L. Energia solar fotovoltaica: panorama e perspectivas para o brasil. *Advir (ASDUERJ)*, 31:7–20, 2013.



POROSITY MEASUREMENT IN B4C-NB COMPOSITE THROUGH DIGITAL IMAGE ANALYSIS AND PROCESSING

Author: Marcos Paulo Dornellas¹ marcosp.dornellas@gmail.com
Advisor(s): Marília Diniz¹

¹ Rio de Janeiro State University

PPG-EM Seminars: season 2021
<http://www.ppgem.uerj.br>

May 11, 2021

Keywords: Advanced ceramics; boron carbide with niobium; porosity; digital image processing.

1 Introduction

Constant research efforts have been conducted in material selection, matching the properties of interest (mechanical, electrical, chemical and thermal), versatility of use, high lifetime and low cost of production. The search for high mechanical performance materials aroused great interest in the enhancement of advanced ceramics such as boron carbide (B4C). However, the porosity is still seen as a performance limiting factor of these ceramics [1].

The difficulty of sintering and the control of porosity still limits ceramic in general. There are many effective techniques for evaluation and quantification of porosity in advanced ceramics, such as computed tomography, however, these techniques require high equipment and handling costs, which led to the search for alternatives that provide equally safe and inexpensive results, as quantitative stereology using the Digital Image Processing (DIP)[2].

Although the boron carbide has attracted considerable attention due to its excellent physicochemical properties, such as hardness (it is the 4rd hardest ceramic), low density (2.52 g/cm³), high melting point (2450 °C), high elasticity modulus, good wear and corrosion resistance, and high neutron absorption ability [3], it has the same difficult about sintering and the control of porosity.

2 Objective

This work aims to quantify the porosity of B4C-Nb sintered at high pressure and temperature (HPHT) through analysis and digital imaging processing techniques (DIP) for images obtained by optical microscopy (OM) and compare with the results found by other methods.

3 Materials and methods

The methodology for some of the main stages of the project will be:

1. Preparation of samples in phenolic resin with sub-

- sequent definition of sanding and polishing parameters;
2. Characterization of surfaces using optical microscopy (MO);
3. Quantitative characterization of material through analysis techniques and digital image processing (PDI);
4. Chemical and morphological characterization of material using scanning electron microscopy (SEM) and semiquantitative chemical analysis by EDS (Energy Dispersive Spectroscopy);
5. Statistical analysis of the results obtained;
6. Comparison of the results obtained using results obtained from other methodologies.

Until now, we have used four samples for each percentage by weight of niobium (2, 5, 10, 20 percent). They were embedded, ground and polished for obtaining optical microscopy images throughout the material. Following collection were 160 images of the surfaces of samples using an optical microscope (MO) Olympus BX60M, 40 for each sample percentage in different regions of the surface. All were collected under 500x magnification. DIP will be carried out through Fiji (It's Just Image J) version 1.53C software.

4 Results and Discussion

As result, from embedded, ground and polished figure 1 illustrates an image obtained by MO 500x magnification. The result after the digital image processing step for extracting and quantifying the number of pores present in the material is the next step to be done.

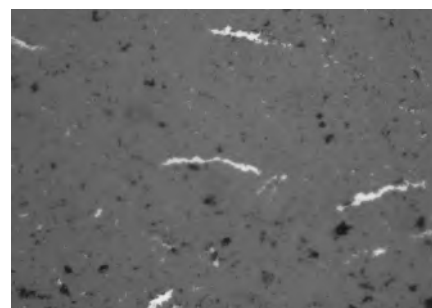


Figure 1: Example of a microstructural aspect obtained in present research for B4C-2% Nb - 500x

The expected results of this project are the following:

- Porosidade analysis of the material;
- Chemical characterization of material to know all phase present;
- Statistical data about porosity;
- Comparative data about porosity with other works;

5 Conclusions

In Addition this work intends to confirm previous studies with the use B₄C-Ni, and similar other works, show that digital image processing had credibility stated for the tested samples, proved to be a suitable method which is based on quantitative metallographic procedures.

References

- [1] Abreu G da S. *Sinterização em alta pressão e alta temperatura (HPHT) do compósito B₄C-Nb*. Tese de doutorado, UENF, Campos dos Goytacazes - RJ, 2019.
- [2] Vinicio C. da Silva. Medida de porosidade em sic através de processamento digital de imagens. Master's thesis, PPGEM/UERJ, Abril 2015.
- [3] Zhang J Ji W Wang W Fu Z Niu B, Zhang F. Ultra-fast densification of boron carbide by flash spark plasma sintering. *Scripta Materialia*, 116:127–130, 2016.



ON THE FICK'S SECOND LAW WITH CONCENTRATION-DEPENDENT DIFFUSION COEFFICIENT

Author: Rogério Pazetto Saldanha da Gama¹
Advisor (s): José Julio Pedrosa Filho¹
¹ Rio de Janeiro State University

rogpaz1998@gmail.com

PPG-EM Seminars, season 2021
[http:// www.ppgem.uerj.br](http://www.ppgem.uerj.br)

June 08, 2021

Keywords: mass transfer, Fick's law, nonlinear phenomenon, Kirchhoff transformation.

Here we introduce the Kirchhoff transformation, within the mass transfer context, as follows

$$\Phi = \hat{\Phi}(c) = \int_0^c \hat{D}(\lambda) d\lambda, \quad D = \hat{D}(c) \quad (3)$$

With the above definition, equation (1) may be rewritten as

$$\frac{1}{D} \frac{\partial \Phi}{\partial t} = \frac{\partial^2 \Phi}{\partial x^2}, \quad x \in (a, b), \quad t > 0 \quad (4)$$

1 Introduction

The diffusion coefficient can be assumed to be a constant in many situations. In particular, the constant diffusion coefficient hypothesis seems to be a good assumption when we study the diffusion of gases.

Nevertheless, when denser fluids are involved, the constant diffusion coefficient hypothesis may lie far from the reality [1,2].

In particular, when the molecular interactions between the diffusing components are not negligible, the diffusion coefficient becomes dependent on the concentration, in a way that the relationship between them should be taken into account.

The main subject of this work is the Fick's second law in a context in which the diffusion coefficient D is a function of the concentration c [3].

In this paper we will restrict our attention to one-dimensional phenomena described by the following nonlinear parabolic partial differential equation

$$\frac{\partial c}{\partial t} = \frac{\partial}{\partial x} \left(D \frac{\partial c}{\partial x} \right), \quad D = \hat{D}(c), \quad x \in (a, b), \quad t > 0 \quad (1)$$

subjected to an initial (constant) data and to Dirichlet boundary conditions. In other words, the concentration c is a function of the spatial position and of the time satisfying (1) and the following conditions

$$\begin{aligned} c &= c_A \text{ (known)} \quad \text{at} \quad x = a, \quad t > 0 \\ c &= c_B \text{ (known)} \quad \text{at} \quad x = b, \quad t > 0 \\ c &= c_0 = \text{constant} \quad \text{for} \quad x \in (a, b), \quad t = 0 \end{aligned} \quad (2)$$

2 The Kirchhoff Transformation

The Kirchhoff transformation is a largely employed tool for helping the description of heat transfer problems in which the thermal conductivity depends on the temperature [4].

in which the diffusion coefficient is, now, regarded as a function of Φ . The functional relationship between the diffusion coefficient and the function Φ is ensured, since the diffusion coefficient is always greater than a given positive constant.

One of the challenges in this work is to present an user friendly relationship between the diffusion coefficient and the concentration, providing an easy way for reaching the concentration c once the function Φ is known.

Now, with the use of the Kirchhoff transformation, the only nonlinearity will be the one due to the diffusivity appearing in the transient term. It is to be noticed that the Kirchhoff transformation works well with discontinuous functions.

This fact induces us to consider piecewise constant relationships between the diffusion coefficient and the concentration.

3 The Piecewise Constant Approximation

The relationship between the diffusion coefficient and the concentration is established from discrete experimental data. So it is always reasonable to consider the diffusion coefficient as a piecewise constant function of the concentration.

In other words, we may write

$$D = \begin{cases} D_1 & \text{for } 0 \leq c \leq c_1 \\ D_i & \text{for } c_i \geq c > c_{i-1}, \quad 1 < i < N \\ D_N & \text{for } 1 \geq c > c_{N-1} \end{cases} \quad (5)$$

in which D_1, D_2, \dots, D_N and c_1, c_2, \dots, c_{N-1} are positive constants

Assuming that the diffusion coefficient is given by (5), the Kirchhoff transformation is given by

$$\Phi = \begin{cases} D_1 c, & \text{if } c \leq c_1 \\ D_2 (c - c_1) + D_1 c_1, & \text{if } c_2 \geq c > c_1 \\ \dots + D_2 (c_2 - c_1) + D_1 c_1, & \text{if } c > c_{N-1} \end{cases} \quad (6)$$

After some calculations, the above relation can be rewritten as follows

$$\Phi = \frac{1}{2} \left((D_1 + D_N) c + \sum_{i=2}^N (D_i - D_{i-1}) (|c - c_{i-1}| - c_{i-1}) \right) \quad (7)$$

Defining the (nonnegative) constants $\Phi_1, \Phi_2, \Phi_3, \dots, \Phi_{N-1}$ as follows

$$\Phi_i = \sum_{j=1}^i D_j (c_j - c_{j-1}), \quad 1 \leq i \leq N-1, \quad \text{with } c_0 = 0 \quad (8)$$

the inverse of the Kirchhoff transformation is unique and explicitly given by

$$c = \frac{1}{2} \left(\left(\frac{1}{D_1} + \frac{1}{D_N} \right) \Phi + \sum_{i=2}^N \left(\frac{1}{D_i} - \frac{1}{D_{i-1}} \right) (|\Phi - \Phi_{i-1}| - \Phi_{i-1}) \right) \quad (9)$$

The above relationship holds for any piecewise constant approximation and, thus, it is completely general.

4 An Example

As an illustrative example, let us consider the following problem,

$$\begin{aligned} \frac{\partial c}{\partial t} &= \frac{\partial}{\partial x} \left(D \frac{\partial c}{\partial x} \right), \quad x \in (0,1), \quad t > 0 \\ D &= \hat{D}(c) = \begin{cases} D_1 = \text{constant}, & 0 \leq c \leq 1/2 \\ D_2 = \text{constant}, & 1/2 < c \leq 1 \end{cases} \\ c &= C_A \quad \text{at } x=0, \quad t > 0 \\ c &= C_B \quad \text{at } x=1, \quad t > 0 \\ c &= 0 \quad \text{for } x \in (0,1), \quad t = 0 \end{aligned} \quad (10)$$

In this case, we have the differential equation written as

$$\frac{1}{D} \frac{\partial \Phi}{\partial t} = \frac{\partial^2 \Phi}{\partial x^2}, \quad x \in (0,1), \quad t > 0 \quad (11)$$

while the boundary conditions are obtained from equation (7), with $c = C_A$ ($\Phi = \Phi_A$ at $x=0$) and with $c = C_B$ ($\Phi = \Phi_B$ at $x=1$).

With the following initial data

$$\Phi = 0 \quad \text{for } x \in (0,1), \quad t = 0 \quad (12)$$

The diffusion coefficient is given by

$$D = D_2 \quad \text{if } \Phi \geq D_1/2; \quad D = D_1 \quad \text{if } \Phi < D_1/2 \quad (13)$$

Denoting by Φ_i^n the approximation for Φ at the time t^n at the position x_i , in which

$$\begin{aligned} x_i &= (i-1)\Delta x, \quad \Delta x = 1/(\bar{N}-1) \\ t^{n+1} &= t^n + \Delta t, \quad t^0 = 0 \end{aligned} \quad (14)$$

we have the following finite difference equations

$$\begin{aligned} \frac{\Phi_i^{n+1} - \Phi_i^n}{D_i^n \Delta t} &= \frac{\Phi_{i+1}^{n+1} - 2\Phi_i^{n+1} + \Phi_{i-1}^{n+1}}{(\Delta x)^2}, \quad i = 2, 3, \dots, \bar{N}-1 \\ \Phi_i^{n+1} &= \Phi_A, \quad \text{for } i = 1 \\ \Phi_i^{n+1} &= \Phi_B, \quad \text{for } i = \bar{N} \\ \Phi_i^0 &= 0, \quad i = 2, 3, 4, \dots, \bar{N}-1 \end{aligned} \quad (15)$$

in which D_i^n is the diffusion coefficient evaluated at the time t^n at the position x_i .

Figure 1 presents some results. In figure 1 we have the case in which $D_1 = 5D_2 = 5D$ represented by the dash dot line, while the case (constant diffusion coefficient) in which $D_1 = D_2 = 3D$ is represented by the continuous thin line.

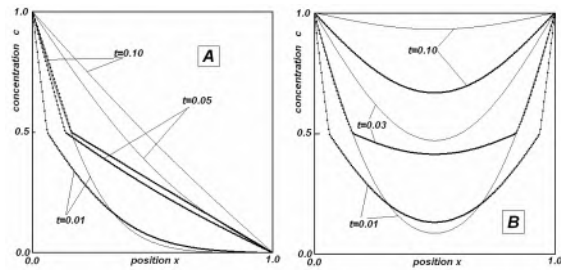


Figure 1: The concentration as a function of the position for three selected times.

References

- [1] C. C. HAN and A. Ziya AKCASU. Concentration dependence of diffusion coefficient at various molecular weights and temperatures. *Polymer*, vol. 22, 1165-1168, 1981.
- [2] R. H. STOKES. One-dimensional diffusion with the diffusion coefficient a linear function of concentration. *Transactions of the Faraday Society*, vol. 48, 887-892, 1952.
- [3] J. C. SLATTERY. *Momentum, energy and mass transfer in continua*. McGraw-Hill Kogakusha, New York, 1972.
- [4] D. GIVOLI. Use of the Kirchhoff transformation in finite element analysis. *International Journal of Numerical Methods for Heat & Fluid Flow*, vol. 3, 463-477, 1993.



ASSESSMENT OF THE DYNAMIC RESPONSE AND FATIGUE ANALYSIS OF STEEL-CONCRETE COMPOSITE FLOORS

Author: Carolina Sanchez Guerrero¹ engenheira.casg@gmail.com
Advisor(s): Francisco Jose da Cunha Pires Soeiro¹

¹ Rio de Janeiro State University

PPG-EM Seminars: season 2021
<http://www.ppgem.uerj.br>

Jul 01, 2021

Keywords: Steel-concrete composite floor; Structural dynamics; Fatigue analysis

1 Introduction

This research work aims the study of the dynamic structural response and evaluates the fatigue response in terms of its structural service life of a steel-concrete composite floor, when subjected to the loading action of mechanical equipment (liquid cooler), the investigated structural system is based on a steel-concrete composite floor. The numerical modelling of the studied composite floor was performed by the ANSYS program, based on the Finite Element Method (FEM). The applied loads were simulated based on harmonic dynamic actions related to the dynamic loadings imposed by the equipment on the structure. The proposed analysis methodology and the procedures presented in the design codes were used to evaluate the floor fatigue response. The conclusions are related to the assessment of the steel-concrete composite floor service life, when subjected to the dynamic actions induced by the mechanical equipment.

2 Model and data presentation

2.1 Structural model

The investigated structural model consists of a steel-concrete composite floor constituted to metallic beams in ASTM A572 Grade 50 Steel and reinforced concrete slab ($f_{ck}=20$ MPa). The main beams and the secondary beams of the structural model are laminated profiles of gauge W360x32.9 and W250x28.4, respectively. The floor has a thickness of 10 cm and measures in plan of 5 m x 5 m, as shown in Figure 1.

2.2 Numerical model

The study was carried out on the position of the equipment in relation to the best use of the composite floor (steel-concrete). As shown in Figure 2, the dynamic loads from the equipment were applied in the equipment support positions on the concrete slab, in the negative direction of the global Y axis. The loads acting on the structural model under study are those used in the structural design; static loads and dynamic loads. The static loads used came from the structure's own weight,

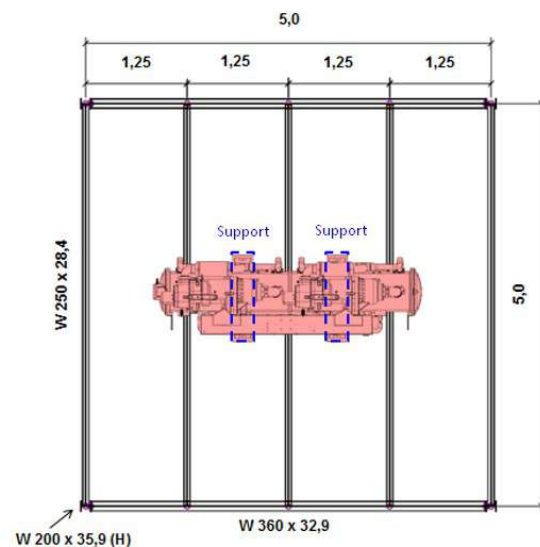


Figure 1: Composite floor (steel-concrete) investigated

the coating on the concrete slab and project overloads. For dynamic loading, dynamic harmonic loads from the 38GPA Condenser Unit equipment, variable over time, were used. A dynamic action generated with the unbalanced motor mass was performed, which was simulated by means of Eq. (1).

$$F(t) = F \sin(\omega t) \quad (1)$$

Where:

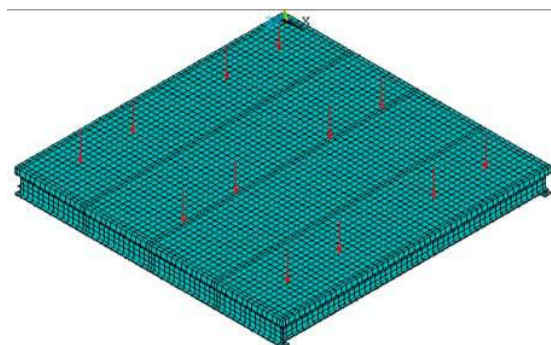


Figure 2: Numerical model with dynamic loading detail

F_0 - Mass of the equipment under study; w - Frequency

of excitation; t - Time.

3 Dynamic response

The dynamic response, in terms of the values of vertical translational displacements, was obtained in the time domain. The node referring to the middle of the span of the composite slab (steel-concrete) is selected, where the maximum values of vertical translational displacements occur. Figure 3 shows the vertical translational displacement response graph in the frequency domain.

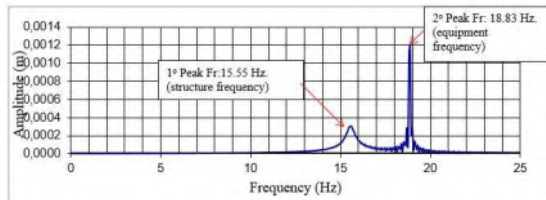


Figure 3: Displacement in the central node of the composite slab in the frequency domain

4 Useful life to fatigue

To determine the service life of fatigue and cumulative damage, it is necessary to obtain the range of stress variation that occurs in the structure during the period of use of the equipment. For this, the history of stresses at the central node was extracted from the ANSYS (2012) program, where the highest stress on the z axis is, as shown in Figure 4, considering all the loads.

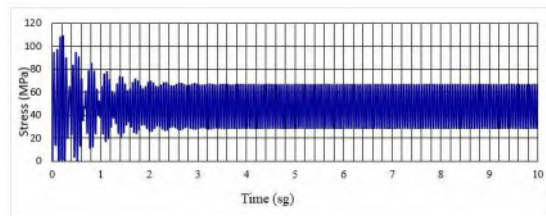


Figure 4: Stress history at the central node of the slab

Fatigue analysis was performed according to the Damage Accumulation Method, based on the Miner-Palmgren rule and the rainflow algorithm, and must be done from the permanent part of the history, so the interval of 7 to 10 seconds was used. Subsequently, the mathematical expressions defined based on the SN curves of each design standard are used (AASHTO, 2012; EUROCODE 3, 2003 and BS - 5400-10.1980), presented in Eq. (2), Eq (3) and Eq. (4), to obtain the accumulated damage and the respective service life of the structural elements.

$$AASHTO : Ni = A(\Delta\sigma_i)^{-m} \quad (2)$$

$$EUROCODE3 : Ni = 10^{\log a - m \log \Delta\sigma_i} \quad (3)$$

$$BS - 5400 : Ni = \frac{K o \Delta^d}{(\Delta\sigma_i)^m} \quad (4)$$

The types of structural details analyzed in this study are identified in Figure 5. Through these parameters and using the formulas of the S-N curve of each one of them, the damage caused by each stress variation is calculated. The lifetime of the structure is the inverse of the sum of the damages.

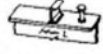
Detalhe Estrutural	Descrição	Norma		
		Eurocode 3	AASHTO	BS 5400
(1)	 Conector laje-viga	Classe 80	Classe C	Classe E
(2)	 Solda de contorno	Classe 63	Classe B	Classe F

Figure 5: Classification of structural details analyzed

Based on what was presented, the fatigue life obtained was 35.9 years according to the AASHTO standard, 4.6 years according to EUROCODE 3 and 15.8 years for the BS-5400 standard. Considering that we must take into account the shortest estimated time, which is small, it is necessary to have an efficient preventive maintenance plan.

5 Conclusions

- For the calculation of the useful life, it is observed that the time obtained by each standard is not the same. This is due to the fact that each one uses a different criterion for their calculation. It can be concluded that the American standard is more conservative, as the calculated service life was longer, and the least conservative of the three is the British one.
- The authors of the research work emphasize the need to study the slab-beam connection in detail, as it is a very complex detail, a parametric study of the different configuration of the equipment can increase the shear forces at these points of the structure.

6 References

- AASHTO, 2012. LRFD Bridge Design Specifications, American Association of State Highway and Transportation Officials (AASHTO), Washington, DC.
- Alencar, G. S., 2015. Análise dinâmica e verificação à fadiga de obras de arte rodoviárias mistas (aço-concreto) submetidas ao tráfego de veículos sobre pavimento irregular. Dissertação de Mestrado. UERJ, Brasil
- Eurocode 3, 2003. Design of steel structures - Part 1-9: Fatigue. European Committee for Standardization.
- Lopes, E. D. C.; et al., 2012 Análise dinâmica não-linear de pisos mistos (aço-concreto) submetidos a ações dinâmicas humanas rítmicas, Rio de Janeiro, Brasil.
- Carrier. Multisplit Alta Capacidade, Unidade condensadora. Catálogo técnico 38GPA-2009.
- NBR 8800, 2008. Projeto de estruturas de aço e de estruturas mistas de aço e concreto de edifícios



SYNTHESIS AND CHARACTERIZATION OF NANOSTRUCTURED HYDROXIAPATITE FOR APPLICATIONS AS CATALYST IN THE PRODUCTION OF BIOFUELS

Author: Adilson Claudio Quizunda¹ adyquizunda@gmail.com
Advisor(s): José Brant de Campos¹

¹ State University of Rio de Janeiro

PPG-EM Seminars: season 2021
www.ppg-em.uerj.br

November 16, 2021

Keywords: Hydroxyapatite, nanometrica, catalyst, ethanol, n-butanol.

1 Introduction

Hydroxyapatite (HAP) is a calcium phosphate, which formulas $\text{Ca}_{10}(\text{PO}_4)_6(\text{OH})_2$, with different properties depending on its mode of preparation [1]. The calcium precursor commonly used to obtain hydroxyapatite is a calcium hydroxide of synthetic or biological origin, such as bovine bones, pig bones, fish bones, shells and fish scale and eggshell [2]. The use of PAH as a catalyst has been increasingly frequent for the conversion of ethanol, as we can see some examples from previous work where the use of PAH had an effect, as for the conversion of ethanol into n-butanol [3], conversion of ethanol to butadiene, using apatites doped with Sb and Mn [4] and used as catalytic reactions. In this work, the eggshell was used to obtain the PAH, a material suggested as an alternative for the evaluation of solid residues; Chicken peel is one of the by-products still undervalued by the industry. In an attempt to dispose of these materials, alternatives are sought for their reuse [5], and one of these alternatives is the use of eggshell to obtain PAH, which will be tested as a catalyst. The present work aims to develop catalysts, using Hydroxyapatite obtained by the sol-gel method, using a leg bark as a matrix for the production of Hydroxyapatite, to be used in the conversion of ethanol into n-butanol [6].

2 Objective

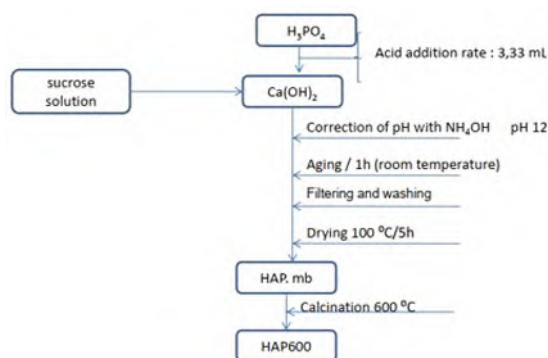
The present work aims to produce, characterize and carry out the catalytic test of hydroxyapatite, obtained from chicken eggshell, using the concentration of sucrose as a porogenic agent, by the sol-gel method, which can be used in the conversion of ethanol in n-butanol.

3 Material and Method

Its use as a catalyst for the manufacture of biodiesel is wide-ranging, with several related works. Another

thriving application is its use as UV protection for polystyrene and nylon, which has protected by minimizing radiation damage and can be used in the textile industry [7]. The PAH that is being characterized was obtained from a combination reaction between $\text{Ca}(\text{OH})_2$ and phosphoric acid (H_3PO_4), using NH_4OH when necessary for pH correction. The products used, with the exception of $\text{Ca}(\text{OH})_2$ were of analytical grade and used without further treatment. The figure 1 presents the synthesis of the process.

Figure 1 – Synthesis process steps.



The TAFA - 8835 thermal spray equipment was used at a pressure of 60 Psi, Amperage - 100, Voltage - 28 - 30 V and compressed air to propel the particles to the substrate. Spraying was performed perpendicularly ($90^\circ \pm 5^\circ$) in Horizontal and Vertical passes with stipulated sprinkling distance between 80 - 120 mm on the surface of the previously prepared sample (Sa 2 1/2 abrasive blasting). After spraying the final thickness of the sample was approximately 8.7mm. Hardness measurements were performed in three different regions of the surface of the coating and in three substrate regions of a sample previously submitted to metallographic preparation, in a total of 6 grids of 30 points each. Roughness measurements were performed through Digital Image Processing (PDI) obtained by Optical Microscopy (OM) and through a roughness gauge of the Digital Surface Profile Gauge | Elcometer 223 - Elcometer USA.

4 Results and Discussion

Our samples were characterized using x-ray, SEM and MET techniques helped to understand how our bifunctional catalyst (acid - base), porosity and surface area between pure HAP and sucrose containing. The Figures 2 and 3 shows the difference between pure HAP and HAP with the porogenic agent, which can be noticed by the way the particles are presented, and it is possible to notice the morphological change of the particles, the sample without the porogenic agent, they are presented in the form of a stick.

Figure 2 - HAPCAS3 and HAP600 with 100,000x magnification.

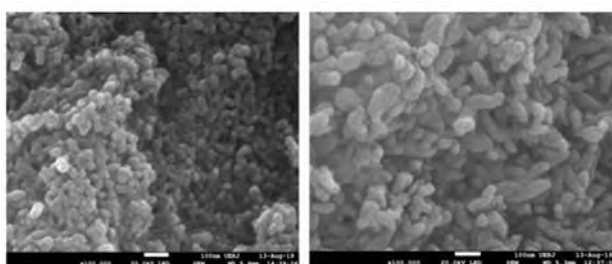


Figure 3 - Brightfield MET image of the HAP600 sample showing rod-shaped morphology.

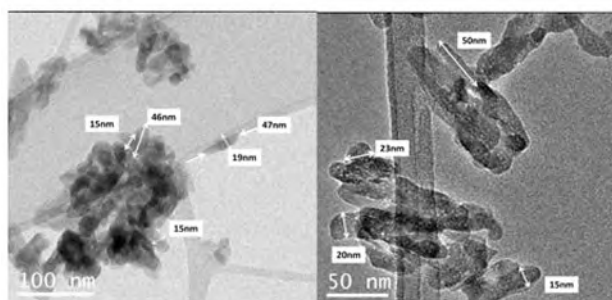
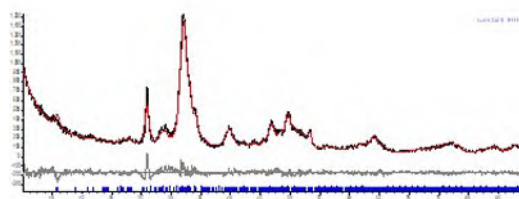


Figure 4 - Diffractogram obtained from the Rietveld method refinement of the HAPCAS3 sample.



5 Conclusions

The HAP obtained contains all the necessary characteristics for application as a catalyst because it has adjustable acid-base properties, low density and a larger surface area when using the porogenic agent, sucrose, directly benefiting the performance of PAH as a heterogeneous catalyst.

References

- [1] R. RAVARIAN, F. MOZTARZADEH, M. SOLATI-HASHJIN, P. KHOSHAKHLAGH, M.TAHRIRI, *Ceramics Introduction*, 2010.
- [2] ROUHANI, P.; TAGHAVINIA, N.; ROUHANI, S.. Rapid growth of hydroxyapatite nanoparticles using ultrasonic irradiation. *Ultrasonics Sonochemistry*, v. 17, n. 5, p. 853-856, 2010.
- [3] S. PRAMANIK, A.K. AGARWAL, K.N. RAI, A. GARG. Nanohydroxyapatite synthesized from calcium oxide and its characterization, *Ceram. Int.* 33 (2007) 419–426.
- [4] KIM, W.; ZHANG, Q.; SAITO, F. Mechanochemical synthesis of hydroxyapatite from Ca (OH) 2-P2O5 and CaO-Ca (OH) 2-P2O5 mixtures. *Journal of materials science*, v. 35, n. 21, p. 5401-5405, 2000.
- [5] OLIVEIRA, D. A.; BENELLI, P.; AMANTE, E. R. Valorizacao de resíduo sólido: cascas de ovos como matéria-prima no desenvolvimento de novos produtos. II International Workshop - Advances in Cleaner Production. Sao Paulo - Brasil, 2009.
- [6] D.P. SERRANO, J.M. CORONADO, V.A. DELA PENA O'SHEA, P. PIZARRO, J.A. BOTAS. Advances in the design of ordered mesoporous materials for low-carbon catalytic hydrogen production, *Journal of Materials Chem. A* 1 (2013) 12016–12027.
- [7] FECHEYR-LIPPENS, D.; NALLAPANENI, A.; SHAWKEY, M. D. Exploring the use of unprocessed waste chicken eggshells for UV-protective applications. *Sustainability*, v. 9, n. 2, p. 232, 2017.



EVALUATION OF THE APPLICATION OF A TIN FILM ON AISI 1045 STEEL TOOLS FOR THE FRICTION STIR WELDING PROCESS, FSW

Author: Bruno Neves Targino Teodoro¹
Advisor(s): José Brant de Campos¹

brunoneves10@yahoo.com.br

¹ Rio de Janeiro State University

PPG-EM Seminars: season 2021
<http://www.ppgem.uerj.br>

November 10, 2021

Keywords: X-Ray Diffraction, Rietveld Refinement, Scanning Electron Microscopy.

AISI 1045 steel substrate, understanding the behavior of the Magnetron technique Sputtering in the material under study.

1 Introduction

Due to the numerous problems that arise in the most common welding processes and the growing concern to reduce the impacts on the environment in the manufacturing processes of consumer goods[3] friction welding process emerged in the 1990s called Friction Stir Welding (FSW), developed by the TWI (The Welding Institute) [4]. This technique has advantages when compared to other more traditional welding methods, such as welding between dissimilar materials, generating low levels of residual stresses and without reaching the melting point of the materials. However, some restrictions limit the even greater use of this technique, and among these factors, the existence of a high level of abrasion and wear to which the tool used is submitted during the entire welding operation stands out. In this work, the evaluation of experimental data of AISI 1045 steel coated with TiN film by the magnetron sputtering technique was carried out, in order to quantify the phases present, by X-ray diffraction, also on the surface of the tools. how to analyze images acquired by scanning electron microscopy to observe the overlay surface characteristics and a discussion of their influence on tool life.

2 Methodology

The methodology that was applied to the present work consisted of refinement steps in the characterization of the AISI 1045 steel sample with TiN film, mainly, focusing on the use of the X-Ray Diffraction (XRD) and Scanning Electron Microscopy (SEM) method, to obtain the desired results. The method employed for the characterization by XRD consisted of the use of software developed to carry out quantitative and qualitative phase analysis, in addition to information on the crystal structure of the sample. During the process, the objective was to extract the most complete and accurate information as possible from the deposited film, in order to obtain satisfactory results on the components that make up the TiN film previously deposited on the

• Qualitative Analysis

The procedure consisted of analyzing the peaks that were not described by Oliveira [2], while the diffraction positions were indicated by the HighScore plus 3.0 program. It was observed in this indicative of the phase selected by the program, which would be compatible with the diffraction planes.

• Quantitative Analysis

The quantitative analysis was based on the Rietveld Refinement Method. The method is based on the simulation of the diffraction profile from the structures of the component phases of a sample, based on calculating the Rietveld equation. In this way it is analyzed the entire diffraction pattern and using the individual intensities of each angular step, the method allows the refinement of complex structures, being possible its application for the provision of data quantitatively precisely. Therefore, the Topas Academic software was used to execute the method. version 4.1, where a search was performed in Inorganic Crystal Structure Database (ICSD), which is the database of crystallographic data, and based on the data obtained previously, the phase with the cubic structure was chosen more suitable for the best fit to occur in the peaks diffracted from the sample.

• Scanning Electron Microscopy (SEM)

The scanning electron microscopy technique was presented by Oliveira [2] and by Neves [1], for the morphological analysis of the surface of tools in which the TiN film was deposited, before and after the friction test, which sought to carry out an analysis of the macro and microstructure of the samples in the regions of greatest effort of the tool. Before the SEM procedure, as a way to evaluate the behavior of the tool in which the TiN film was deposited, Oliveira [2] carried out tests of adhesion of the film to the substrate, which consisted of a test of the friction welding process, a technique called of FSP, Friction Stir Process, where

the equipment to carry out the FSW welding is used, however, the welding between plates is not carried out. In this technique, FSP, the tool is penetrated in 0.3 mm in a single Al plate, specimen, with a penetration speed of 4 mm/min and performs a 20 mm travel.

3 Results

3.1 X-Ray Diffraction

The results obtained through the X-Ray Diffraction analysis were analyzed using two software. HighScore Plus 3.0 (Pannalytical) for a qualitative analysis, and Topas Academic version 4.1 (Bruker) to obtain quantitative results, using the Rietveld Refinement Method. Some of the refined data were: Grid parameters, crystallite size and scale parameters.

To carry out the indexing of the phases present in the sample, the crystallographic records of the Inorganic Crystal Structure Database (ICSD) databases were used. All the files consulted had Star, Indexed or Calculated quality, in order to guarantee the quality of the reference data for the analysis. The crystallographic chips used for the determined phases were: - TiN, ICSD 64907; - Fe, ICSD 166536; - $\text{Ti}_{10}\text{Fe}_{7}\text{N}_{10}\text{O}_{33}$, ICSD 426340; - Ti_2N , ICSD 33715; - TiFe_2O_4 , ICSD 9806. Thus, it was possible to achieve an excellent Goodness Of Fit (GOF) adjustment value in the characterization of the sample, very close to the value of 1.13.

The following result was then reached in the general characterization of the present phases:

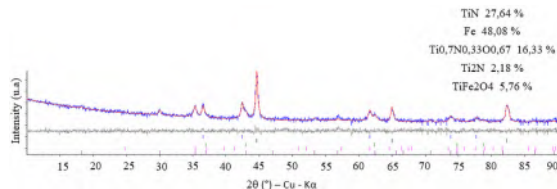


Figure 1: Adjustment for the determination of phases by the Rietveld Method of the sample with coating deposition.

In the image below, it is possible to verify the phases present in the TiN film that were found with the proper Rietveld refinement parameters specified. Bringing essential information on the microstructural aspects of the deposited film, such as the crystal structure of each phase, density, crystallite size and lattice parameters.

FORMED PHASE	CRYSTALLINE STRUCTURE	DENSITY [g/cm ³]	CRYSTALLITE SIZE [nm]	NETWORK PARAMETERS [Å]
TiN	Cubic	5,34	35,83	4,25
Fe	Cubic	7,86	64,13	2,86
$\text{Ti}_{10}\text{Fe}_7\text{N}_{10}\text{O}_{33}$	Cubic	4,36	21,63	4,2
Ti_2N	Tetragonal	5,13	23,46	5,07 ; 2,75
TiFe_2O_4	Cubic	4,99	30,91	8,41

Figure 2: Refinement parameters obtained by Rietveld.

3.2 Scanning Electron Microscopy (SEM)

Images referring to the lateral surface of the "pin" near the end of the piece were presented, as well as images

close to the "shoulder" of the piece. These parts were chosen to carry out the analysis because they were the regions with the greatest demands in the welding process to which the part would be submitted.

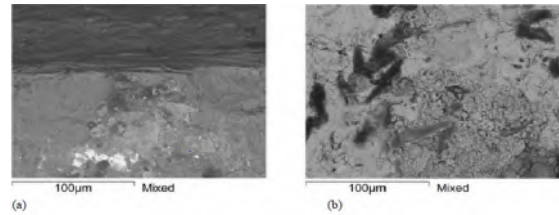


Figure 3: Scanning electron microscopy of samples with TiN film, 800X magnification. (a) end of specimen and (b) shoulder of specimen.

Thus, through the analysis of the images obtained from the SEM, it is possible to identify the pullout of the TiN film at the end of the tool.

4 Conclusions

Here, you will end up your text by drawing conclusions and comments about future work. In order to reduce the contents, we encourage you to summarize the main results by using an itemised list as follows:

- The characterization of the TiN film phases was performed satisfactorily (GOF: 1.13);
- Two new phases were identified and quantified in relation to previous studies: Ti_2N 2.18% and TiFe_2O_4 5.76%;
- A collection of all SEM images obtained in previous works was carried out where the scarcity of the film at the end of the tool was observed;

References

- [1] H. H NEVES. Avaliação da aplicação do filme de tin em ferramenta de aço aisi 1045 para o processo de soldagem por atrito, fsw, 2019.
- [2] OLIVEIRA Paulo Rodrigues. Avaliação do recobrimento de tin aplicado em ferramenta de aço aisi 1045 para o processo de soldagem por atrito, fsw. Master's thesis, UERJ, 2018.
- [3] MISHRA. R. S and MA. Z. Y. Friction stir welding and processing. *Materials Science and Engineering*, 50:1–78, 2005.
- [4] Wayne M. et al THOMAS. *Friction stir butt welding*. Welding Institute England, 1995.



DYNAMIC ANALYSIS OF BUILDINGS CONSIDERING THE EFFECT OF MASONRY INFILLS

Author: Carolina S. Guerrero¹ engenhaira.casg@gmail.com
Advisor(s): Francisco Jose da Cunha Pires Soeiro¹

¹ Rio de Janeiro State University

PPG-EM Seminars: season 2021
<http://www.ppgem.uerj.br>

Nov 17, 2021

Keywords: Nondeterministic Dynamic Analysis; Concrete Buildings; Masonry Infill ; Human Comfort.

1 Introduction

This research work presents a study that aims to assess the dynamic structural behaviour and also investigate the human comfort levels of a reinforced concrete building, when subjected to nondeterministic wind dynamic loadings, considering the effect of masonry infills on the global stiffness of the structural model. In general, the masonry fills most of the empty areas within the structural frames of the buildings. Although these masonry infills present structural stiffness, the common practice of engineers is to adopt them as static loads, disregarding the effect of the masonry infills on the global stiffness of the structural system. This way, in this study a numerical model based on sixteen storey reinforced concrete building with 48 m high and dimensions of 14.20 m x 15 m was analysed. This way, static, modal and dynamic analyses were carried out in order to simulate the structural model based on two different strategies: no masonry infills and masonry infills simulated by shell finite elements. In this investigation, the wind action is considered as a nondeterministic process with unstable properties and also random characteristics. The fluctuating parcel of the wind is decomposed into a finite number of harmonic functions proportional to the structure resonant frequency with phase angles randomly determined. The nondeterministic dynamic analysis clearly demonstrates the relevance of a more realistic numerical modelling of the masonry infills, due to the modifications on the global structural stiffness of the building.

2 Nondeterministic Wind Mathematical Modelling

Wind properties are unstable, have random variation, and thus, their deterministic consideration becomes inadequate. However, it can be considered that for generation of nondeterministic dynamic loading time series it is assumed that the wind flow is unidirectional, stationary and homogeneous. This implies that the direction of the main flow is constant in time and space, and that the statistical characteristics of the wind do not

change during the period in which the simulation is performed (Obata, 2009). This way, in this investigation, the wind dynamic loadings are considered combined into a turbulent part (nondeterministic dynamic load) and another static parcel (mean wind force). The turbulent part of the wind is decomposed into a finite number of harmonic functions, with randomly determined phase angles. The amplitude of each harmonic is obtained based on the use of a wind power spectrum function, as illustrated in Figure 1.

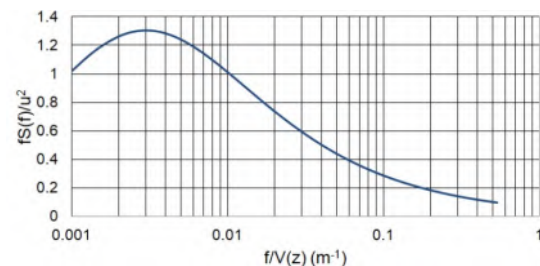


Figure 1: Kaimal Power Spectral Density

3 Investigated Reinforced Concrete Building

The investigated building in this research work presents rectangular dimensions of 15.00 m by 14.20 m, is composed by 16 floors, with a height of 3.0 m, having a total height of 48 m, as shown in Figure 2. The reinforced concrete structure of the building consists of massive slabs with a thickness equal to 10 cm, girders with sections 12 x 50 cm and columns with two sections dimensions: 20 x 80 cm, and 30 x 150 cm. The building is residential with two apartments per floor, four elevators, located at the city of Rio de Janeiro/RJ, Brazil.

Two structural models were developed in this research work. The so called Model 1 (M1) that consists of the reinforced concrete structure only (girders, slabs and columns) and the Model 2 (M2) which presents the same structural system of the first model, however the masonry infills were considered in the modelling, aiming to evaluate the global stiffness of the building.

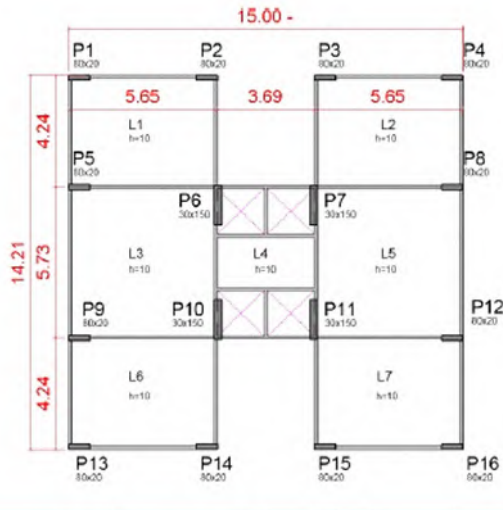


Figure 2: Investigated reinforced concrete building (units in meters)

4 Global stiffness of the investigated building

According to Figure 3, it is possible to conclude that the consideration of masonry infills in the numerical models M1 and M2 directly influences the results regarding the global stiffness and the horizontal translational displacements values, due to the application of the unit load. In this situation, Model 2 presents a global stiffness 453% higher in the X direction and 617% higher in the Z direction when compared to Model 1.

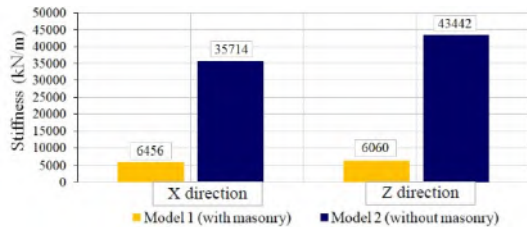


Figure 3: Comparison between the global stiffness in X and Z directions of the FEM M1 and M2

5 Nondeterministic Dynamic Analysis

The results of the dynamic analysis for the maximum horizontal translational displacements values are obtained at the top structural sections of the building (nodes in the FEM: $h = 48$ m), and for the maximum accelerations these values are calculated at the floor of the last building storey ($h = 45$ m). In this research work 30 nondeterministic wind series were generated, considering the two horizontal displacements in the X and Z axes, for each FEM M1 and M2, respectively. Based on the Table 1 results, it can be seen that the maximum translational horizontal displacements values calculated at the top of the building ($h = 48$ m), associated to the X and Z directions, are equal to 6.1 cm and 5.4 cm, respectively [Model 1 (M1)]; and equal to 0.9 cm and 0.6 cm, respectively [Model 2 (M2)]. It can be concluded that Model 2 presents displacements values

about 6.0 times higher in X direction and 10 times higher in Z direction when compared with the Model 1 structural response, as shown in Table 1. On the other hand, the maximum acceleration values calculated at the floor of the last building storey ($h = 45$ m), related to the X and Z directions, are equal to 0.32 m/s^2 and 0.31 m/s^2 , respectively [Model 1 (M1)]; and equal to 0.16 m/s^2 and 0.18 m/s^2 , respectively [Model 2 (M2)]. It is possible to notice that the accelerations obtained with Model 2 are almost 2 times higher in the X and Z directions than in Model 1.

Table 1: Mean maximum peak accelerations values associated to the X and Z directions: FEM M1 and M2

Direction	Model	Displ. (cm)	Accel. (m/s^2)
X	M1	0.61	0.16
X	M2	6.07	0.31
X	M1/M2	9.95	1.94
Z	M1	0.90	0.18
Z	M2	5.04	0.32
Z	M1/M2	5.60	1.80

6 Conclusions

The main conclusions of the present investigation are:

- Global stiffness: Static analyses have shown that the presence of the masonry infills in the numerical modelling have increased the building global lateral stiffness around 453% in the X direction and 617% in the Z direction.
- Forced vibration: Based on the nondeterministic dynamic analysis, it was possible to verify the significant decrease of 6 times in the X direction and 10 times in the Z direction of the displacements values at the top of the building when the masonry infills were considered. The accelerations values also have presented a decrease around 2 times when the masonry was considered in the analysis.
- Human comfort: When the human comfort assessment was considered in this investigation, it was concluded that even having in mind that the presence of the masonry infills cause the decrease of the peak accelerations, the user of the building will sense the wind vibrations, based on the Brazilian standard NBR 6123 (1988) criterion.

7 References

- Obata, S.H. (2009), "Vento sintético e a simulação de Monte Carlo - uma forma de considerar a característica aleatória do carregamento dos ventos em estruturas", *Exacta*, 7, 77-85.
- NBR 6123 (1988), Forças devidas ao vento em edificações (In Portuguese), Associação Brasileira de Normas Técnicas (ABNT), Rio de Janeiro, Brasil.



NONLINEAR HEAT TRANSFER STUDY IN RADIAL POROUS FINS

Author: Jonatas Motta Quirino¹ quirinojm@hotmail.com
Advisor(s): Eduardo Dias Corrêa¹

¹ Rio de Janeiro State University

PPG-EM Seminars: season 2021
<http://www.ppgem.uerj.br>

Nov 17, 2021

Keywords: Nonlinear heat transfer, Porous media, from Numerical simulation, Sequence of linear problems

1 Introduction

In general, the first choice for the enhancement of rate of heat transfer from/to a body consists of using fins. Since the need of optimizing heat transfer processes is encountered in several practical situations, the study of the thermal behavior of fins becomes a fundamental issue in the heat transfer area.

The extended surface is widely used in several engineering systems as show recent studies [1] and [4]. Usually, convection and conduction heat transfer are the main considered mechanisms, but radiation heat transfer has significant effect in specifics applications mainly involving high temperatures and/or rarefied atmospheres [3].

2 Mathematical model

The modelling of heat transfer that occurs in a porous radial fin comprises such an analysis considering the material that constitutes the fin as being isotropic and homogeneous, in addition to the fin being analyzed as a strict heat sink, as exemplified in Fig. 1.

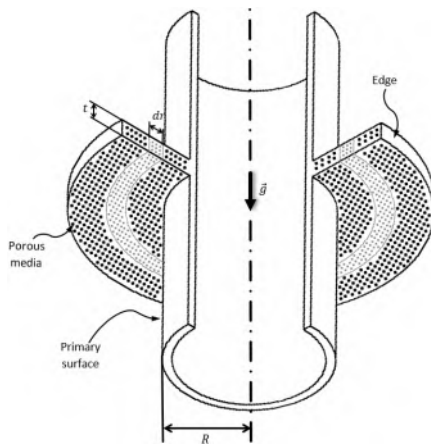


Figure 1: Radial porous fin.

Analyzing the fin as a porous medium leads to infiltration of the fluid in which the fin is inserted, thus allowing a greater exchange of heat between them. The general heat exchange equation used in this work arises

$$q(x) - q(x + \Delta x) = \dot{m}c_p [T(x) - T_\infty] + hP\Delta x[T(x) - T_\infty] + P\Delta x\sigma\varepsilon \left[T^4(x) - \frac{\alpha_f}{\varepsilon} T_\infty^4 \right] \quad (1)$$

Evaluating at $\Delta x \rightarrow 0$, and assuming that $\alpha_f = \varepsilon$, we can rewrite Eq. 1, adapting it to cylindrical coordinates, such as

$$\frac{1}{r} \frac{d}{dr} \left(r \frac{dT}{dr} \right) - \frac{\rho_f g \beta_f K}{\nu_f k_{eff} t} (T - T_a) - \frac{2\varepsilon\sigma F_{f-a}}{k_{eff} t} (|T|^3 T) = 0 \quad (2)$$

The term $|T|^3 T$ is used to ensure coerciveness, since the function for the temperature T is strictly increasing. [2]

By rearranging the equation so that its algebraic manipulation is convenient, you can rewrite Eq. (3) as

$$\frac{d^2 T}{dr^2} + \frac{1}{r} \frac{dT}{dr} - A[|T - T_\infty|(T - T_\infty)] - B[(|T|^3 T) - T_\infty^4] = 0 \quad (3)$$

where the constant A gathers all flow and geometric parameters that affect the solution of the problem and B characterizes the radiation parameter, which carries the effects of the porous body's emissivity.

The temperature values and the geometric position values will be dimensionless through the following relationships:

$$\theta = \frac{T(r)}{T_b} \quad (4)$$

$$\xi = \frac{r}{R} \quad (5)$$

This equation is considered by being subject to the following boundary conditions

$$\xi = 1 \rightarrow \theta = T_b = 1 \text{ (base)} \quad (6)$$

$$\xi = R \rightarrow \frac{d\theta}{d\xi} = 0 \text{ (tip)} \quad (7)$$

3 Results

The problem is modelled as

$$\frac{1}{\xi} \frac{d}{d\xi} \left(\xi \frac{d\varphi^{(i+1)}}{d\xi} \right) - \alpha \varphi^{(i+1)} + \beta^{(i)} = 0 \quad (8)$$

with

$$\beta^{(i)} = \alpha \varphi^{(i)} - A \left| \varphi^{(i)} - T_\infty \right| (\varphi^{(i)} - T_\infty) - B \left[|\varphi^{(i)}|^3 \varphi^{(i)} - T_\infty^4 \right] \quad (9)$$

that has, as its solution the limit of the sequence $[\varphi^0, \varphi^1, \varphi^2, \varphi^3 \dots]$, where we chose to use the Finite Difference Method to solve the ODE.

Thus, the numerical model adopted becomes

$$\varphi_n^{(i+1)} = \frac{l}{2 + \alpha l^2} \left[\frac{\varphi_{n+1}^{(i+1)} + \varphi_{n-1}^{(i+1)}}{l} + \frac{\varphi_{n+1}^{(i+1)} - \varphi_{n-1}^{(i+1)}}{2\xi_n} + \beta_n^{(i)} l \right] \quad (10)$$

where

$$\beta_n^{(i)} = \alpha \varphi_n^{(i)} - \left[A |\varphi_n^{(i)} - T_\infty| (\varphi_n^{(i)} - T_\infty) - \left[B (|\varphi_n^{(i)}|^3 (\varphi_n^{(i)} - T_\infty^4)) \right] \right] \quad (11)$$

Therefore, it can be understood that i is the index that represents the numerical iteration comprising each element of the sequence whose limit is the solution to the problem.

Meanwhile, n is the index that represents the numerical iterations of each point in space (geometric) along the radial fin.

It is possible to better visualize how the parameters of Temperature, Sequence Elements and Fin Nodal Points vary in a combined way through the Figure 2.

Thus, as expected, it is noted that convergence occurs more quickly at points closer to the base.

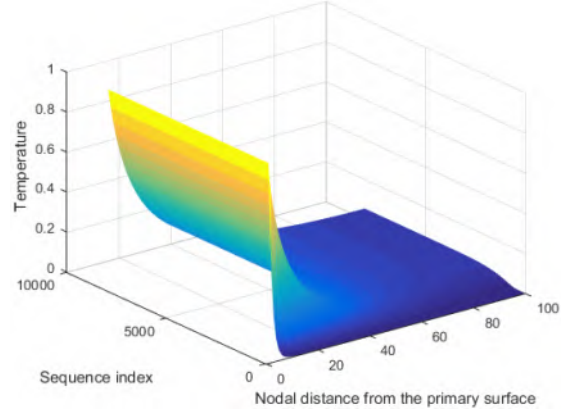


Figure 2: Result surface.

4 Conclusions

This work provides a comprehensive approach to heat dissipation in extended surfaces, where several parameters were considered, among which the application of thermal radiation effects and the porosity of the fin material stand out.

Several works that investigate the thermal behavior of fins neglect a deeper study of the influence of the fins. This work seeks an adequate solution to the problem, applying a cylindrical geometry, which is widely used in engineering situations, mainly in heat dissipation in industrial pipes.

Furthermore, this work presents a numerical solution using simple methods that can be replicated for other analyzes in the future, where factors such as the porosity parameter, other fin geometries, or even variation in the thermal phenomena used can be studied in greater depth.

References

- [1] A Arulselvan, V Pandiyarajan, and Ramalingam Velraj. Experimental investigation of the thermal performance of a heat pipe under various modes of condenser cooling. *Heat Transfer Research*, 48(13), 2017.
- [2] Rogério Martins Saldanha da Gama. Existence uniqueness and construction of the solution of the energy transfer problem in a rigid and nonconvex black body. *Zeitschrift für angewandte Mathematik und Physik ZAMP*, 42(3):334–347, 1991.
- [3] J. M. Quirino, E. D. Correa, R. L. Sobral, and R. M. S. da Gama. The kirchhoff transformation for convective-radiative thermal problems in fins. *International Journal of Mechanics*, 15:12–21, 2021.
- [4] Giulia Righetti, Claudio Zilio, Simone Mancin, and Giovanni A Longo. Heat pipe finned heat exchanger for heat recovery: results and modeling. *Heat Transfer Engineering*, 39(12):1011–1023, 2018.



NUMERICAL SIMULATION OF TRANSPORT THROUGH POLYMER LAYER AND POROUS ARTERIAL WALL OF SIROLIMUS AND PACLITAXEL IN DRUG-ELUTING STENTS

Author: Haroldo Rosman¹ haroldo.rrj@gmail.com
Advisor(s): Norberto Mangiavacchi and Rachel Lucena¹

¹ Rio de Janeiro State University

PPG-EM Seminars: season 2021
<http://www.ppgem.uerj.br>

November 10, 2021

Keywords: drug-eluting stents, Darcy's law, convection-diffusion-reaction equations, Finite Element Method.

1 Introduction

Close to 40% of cardiovascular disease deaths are due to coronary artery disease (CAD). The CAD is the result of obstruction of the coronary arteries and one of the most popular treatment for this disease is to employ a stent - a tiny expansible wire tube that is inserted in the obstructed coronary artery to maintain widen the lumen. The drug-eluting stents (DES) are widely used, which are coated with a polymer that slowly releases a drug. This paper aims to analyze the drug elution from the polymer coating, transport, specific and non-specific binding in the artery wall for sirolimus and paclitaxel drugs. The elution for two different release regimes, fast and slow, associated with two different polymer diffusion coefficients was analyzed. Simulations performed with the developed computational model allow to fine-tune the polymer diffusion coefficient, and other geometric tunable parameters, in order to obey the required restraints for a safe DES utilization.

2 The Mathematical Model and Numerical Method

Figure 1-(left) shows the model geometry where z direction is the axis of symmetry and r is the radial direction. Using the Gmsh - a mesh generator tool - we create a two-dimensional unstructured triangular mesh, as shown in Fig. 1-(right), which is used in the simulations.

We adopt the modeling framework of [1] and [3]. The arterial wall and the polymer layer are considered as porous media, and flow within these layers is assumed to be governed by Darcy's law and to be incompressible, $\nabla \cdot \mathbf{u} = 0$, thus,

$$\nabla \cdot \left(-\frac{P_{D_i}}{\mu} \nabla p \right) = 0, \quad (1)$$

where $\mathbf{u} = (u, v)$ is the velocity field with radial and axial components, respectively, p is the pressure in

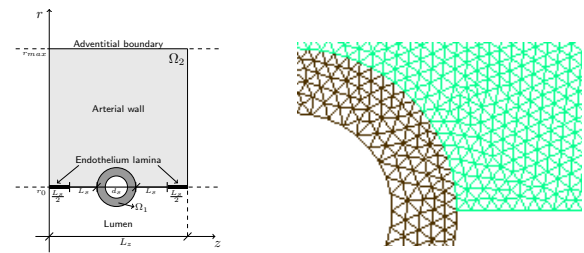


Figure 1: Left: Model 2D axisymmetric geometry. Right: Computational domain and unstructured triangular mesh. Black: polymer layer Ω_1 . Green: arterial wall Ω_2 .

the arterial wall, P_{D_i} is the Darcy permeability of the media and μ is the fluid viscosity. The drug dynamics in the coating is modeled in terms of b_0 (solid) and c_0 (dissolved) concentrations by the equations:

$$\frac{\partial b_0}{\partial t} = -\beta_0 b_0^{2/3} (S_0 - c_0) \quad (2)$$

$$\frac{\partial c_0}{\partial t} + \mathbf{u}_s \cdot \nabla c_0 = \nabla \cdot (\mathcal{D}_0 \nabla c_0) + \beta_0 b_0^{2/3} (S_0 - c_0), \quad (3)$$

where $\mathbf{u}_s = \mathbf{u}/\phi_i$ is the seepage velocity, and ϕ_i is the effective porosity of the media, \mathcal{D}_0 is the effective scalar diffusion coefficient of the solute, β_0 the dissolution rate and S_0 is the solubility limit. Drug elution in the arterial wall is governed by the convection-diffusion-reaction equations:

$$\frac{\partial c_1}{\partial t} + \mathbf{u}_s \cdot \nabla c_1 = \nabla \cdot (\mathcal{D}_1 \nabla c_1) - k_1^f c_1 (b_1^{max} - b_1) + k_1^r b_1 - k_2^f c_1 (b_2^{max} - b_2) + k_2^r b_2 \quad (4)$$

$$\frac{\partial b_1}{\partial t} = k_1^f c_1 (b_1^{max} - b_1) - k_1^r b_1 \quad (5)$$

$$\frac{\partial b_2}{\partial t} = k_2^f c_1 (b_2^{max} - b_2) - k_2^r b_2, \quad (6)$$

where c_1 is the concentration of a drug transported in the arterial wall, b_1 and b_2 denote non-specifically and specifically bound drug, respectively. The effectiveness of the drug delivery depends on the specifically bound concentration. The k_i^f, k_i^r, b_i^{max} are constant parameters related to the binding kinetics, and \mathcal{D}_1 is the

diffusion coefficient, given by an anisotropic tensor,

$$\mathcal{D}_1 = \begin{bmatrix} \mathcal{D}_{1rr} & \mathcal{D}_{1rz} \\ \mathcal{D}_{1zr} & \mathcal{D}_{1zz} \end{bmatrix}, \quad (7)$$

with r the radial direction and z the axial direction. The permeability in the polymer coating, P_{D0} , is considered to be very small, but finite. The endothelium lamina, where present, is modeled as a no-flow boundary. The boundary conditions for drug concentration in the denuded endothelium is $c_1 = 0$, between polymer and lumen, i.e., on interface Γ_1 is $c_0 = 0$, and in the interior surface of Ω_1 , we impose zero flux (see Fig. 1(left)). We assume periodic conditions at the side boundaries.

The mass flux is established across the interface and the drug starts to be transferred to the adjacent release medium. The instantaneous flux and the mass flux (integral) is given, respectively, by:

$$\varphi_i(t) = \int_{\Gamma_i} \mathbf{n} \cdot \mathcal{D}_0 \nabla c_0(t) d\Gamma, \quad \text{with } i = 1, 2, \quad (8)$$

$$\Phi_i = \int_0^t \varphi_i(t) dt, \quad (9)$$

where $i = 1$ refers to the lumen interface, $i = 2$ to the arterial wall, \mathbf{n} is the surface normal, $d\Gamma = 2\pi r d\theta$ and t is the time. The governing equations in 2D axisymmetric coordinates are solved on an unstructured triangular mesh, using linear base functions and the Galerkin Finite Element Method [see 2]. The convective terms are discretized using a semi-Lagrangian approach. A semi-implicit fractional step method is employed for the convection–diffusion–reaction equations. All the simulations were performed with an in-house code, which was written in Octave language.

3 Computational Results and Discussion

The pressure and velocity distributions are assumed constant along the simulation of both drugs transport. In the beginning of the simulation all the drug is in solid form, contained in the polymer layer, with concentration B_0 , and null concentration elsewhere. For both drugs, the solid gradually dissolves in the polymer layer and diffuses to the porous artery wall.

The fast regime release was simulated for 20 days and the Fig. 2 shows the results for both drugs at the second day for the concentration c_1 in the arterial wall. We can observe that in 2 days the drug starts to leave the stent and penetrate the arterial wall with an even greater concentration near the stent, and it is a little faster for paclitaxel.

Figure 3 shows the instantaneous and integral mass flux, for both drugs, through the arterial wall and lumen. We can observe that for the instantaneous mass flux curves the behaviors are similar, decreasing fast until the third day and slowly down to zero at the day fifteen. The mass flux has a curve with a similar gradient for arterial wall and lumen. However, for both drugs the mass flux is bigger to the arterial wall than to the lumen.

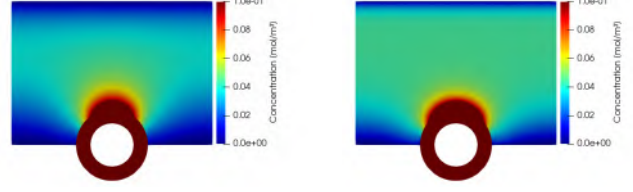


Figure 2: Concentration c_1 in the fast regime for sirolimus and paclitaxel at the day 2 (left and right).

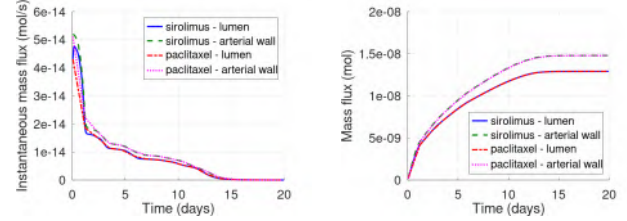


Figure 3: Comparison of the instantaneous mass flux (left) and mass flux in the arterial wall and lumen for fast regime release (right).

4 Conclusions

Paclitaxel and sirolimus have a similar dissolution and diffusion behaviors. The more uniform distributions of free and bound paclitaxel can be explained by the more anisotropic diffusion, with larger axial direction diffusion of paclitaxel compared with sirolimus. Regarding the free concentration c_1 and the solid bound concentration b_0 , sirolimus and paclitaxel have similar curves for both regimes. The two drugs have almost the same behavior for both fast and slow regimes regarding the mass flow and the instantaneous mass flow, since these are mostly controlled by the dissolution rate. For the purposes of this study we assumed that the binding parameters of paclitaxel match those of sirolimus. This is a limitations that will be addressed in future work.

5 Acknowledgments

The authors would like to acknowledge financial support from FAPERJ, CAPES, CNPq, and the University of Glasgow EPSRC GCF ISF fund.

References

- [1] F Bozsak, JM Chomaz, and AI Barakat. Modelling the transport drugs of eluted from stents: physical phenomena driving drug distribution in the arterial wall. *Biomech Model Mechanobiol*, 13:327–347, 2014.
- [2] R.M. Lucena, N. Mangiavacchi, J. Pontes, G. Anjos, and S. McGinty. On the transport through polymer layer and porous arterial wall in drug-eluting stents. *Journal of the Brazilian Society of Mechanical Sciences and Engineering*, 40(572), 2018.
- [3] S McGinty and G Pontrelli. On the role of specific drug binding in modelling arterial eluting stents. *J Math Chem*, 54:967–976, 2016.



SEALANT WITH SILVER ADDITIVE AND ITS EFFECTIVENESS IN COMBATING HOSPITAL BACTERIA

Author: Ully Guimarães Rocha¹ rocha.ully@posgraduacao.uerj.br
Advisor(s): Daniel José Nahid Mansur Chalhoub¹

¹ Rio de Janeiro State University

PPG-EM Seminars: season 2021
<http://www.ppgem.uerj.br>

Dec 17, 2021

Keywords: Silver Based Sealants, In Vitro Tests, Antimicrobial.

1 Introduction

The globalization of microorganisms has gained evidence recently. With air travel, an infected individual can travel around the world in a short period. In other words, a simple trip can infect an entire world, turning an epidemic into a pandemic with surprising speed[5].

Considering environments of possible spread of diseases or infections, when not taken care of, hospitals are focal points for pathogenic microorganisms [4]. With a high mortality, this type of infection creates a big impact and concern in the medical field [1].

As an attempt to combat the proliferation caused by contamination of surfaces such as stretchers, tables, switches, and hospital materials, research proven the biocidal activity of some materials, like silver, copper, zinco and others. Silver is one of the most toxic metals for bacteria and, based on that, we will study the in vitro tests to analyze the influence of sealants based on Silver applied on thermoplastic polymers obtained by 3D printing in the reproduction of bacteria [2, 3, 6].

2 Objective

The project consists of manufacturing a coating-composed silver, forming a paint or varnish, to be applied on hospital surfaces, with the objective of reducing the development of bacteria. The use of this coating would be, primarily, in PPE, beds and general equipment used in hospitals. Thus, building a protective layer that prevents the proliferation of bacteria in these environments. The ideal result, for this study, would be the reach of a material that would definitively eliminate the existence of bacteria, and something like them. The coating will be studied through measurements and analysis of roughness, in vitro tests and other parameters of the covered surface.

3 Materials and methods

The coating will be studied through the following measurements:

1. Chemical and morphological characterization of surfaces and seal coatings using optical microscopy (MO), scanning electron microscopy (SEM) and semiquantitative chemical analysis by EDS (Energy Dispersive Spectroscopy);
2. Quantitative characterization of coatings and colonies of bacteria adhered to In Vitro Tests through analysis techniques and digital image processing (PDI);
3. In vitro tests that simulate the growth environment of bacteria and viruses in the hospital environment;
4. Statistical analysis of the results obtained.

3.1 Parameters

The polylactide (PLA), material that will be coated by sealant fabricates with the following parameters:

1. Temperature: 210;
2. Print speed: 35 mm/s;
3. External wall printing speed: 17.5 mm/s;
4. Print speed of the first and last layer: 17.5 mm/s;
5. Layer height: 0.3 mm;
6. Line width: 0.48 mm;
7. Number of walls: 2;
8. Base layers: 3;
9. Top layers: 3;
10. Filling density: 10.

4 Results

From a bibliographic survey is expected with the preparation of a technical scientific report equipped with methodology and that serves as an instrument for the characterization for samples covered with sealants and Mastery of characterization techniques on macro, micro and nano scales for protective sealing coatings. But the most important result expected is the effectiveness in combating silver as an antibacterial and, for this measure, we will use statistical and comparative data on bacterial growth.

5 Conclusions

In addition this work intends to confirm previous studies with the use of Silver as an antimicrobial tested in hospitals, to verify the effectiveness of this material, possible toxicity, manufacture, and use of another

barrier against hospital bacteria, being in the future a possibility for further studies, fabrications, or alterations with other types of materials with the use of this sealant whose initial idea is to open studies between engineering and the health area.

6 Acknowledgments

This study was financed in part by the Coordenação de Aperfeiçoamento de Pessoal de Nível Superior - Brasil (CAPES) - Finance Code 001, the advisor of this research D.Sc. Daniel José Nahid Mansur Chalhoub, the co-advisor D.Sc. Marília Garcia Diniz, partnership with the Laboratory of Microbiology at the UFRJ.

References

- [1] Neusa de Queiroz Santos. A resistência bacteriana no contexto da infecção hospitalar. *Texto & Contexto-Enfermagem*, 13:64–70, 2004.
- [2] Costi D Sifri, Gene H Burke, and Kyle B Enfield. Reduced health care-associated infections in an acute care community hospital using a combination of self-disinfecting copper-impregnated composite hard surfaces and linens. *American journal of infection control*, 44(12):1565–1571, 2016.
- [3] Fernanda Torres de Souza et al. Caracterização da superfície de pla produzido por manufatura aditiva com selante antimicrobiano para uso na confecção de epi. 2021.
- [4] Ruth Natalia Teresa Turrini. Infecção hospitalar e mortalidade. *Revista da Escola de Enfermagem da USP*, 36:177–183, 2002.
- [5] Stefan Cunha Ujvari. A história da disseminação dos microrganismos. *estudos avançados*, 22(64):171–182, 2008.
- [6] Patricia Lalueza Valero. *Materiales inorgánicos nanoestructurados basados en plata. Aplicaciones bactericidas*. PhD thesis, Universidad de Zaragoza, 2013.



DETERMINATION OF THERMAL CONDUCTIVE OF POLYMERIC MATRIX NANOCOMPOSITES WITH GRAPHENE OXIDE CHARGES BY HOT PLARE METHOD

Author: William Montijo de Oliveira¹ william.montijo@hotmail.com
Advisor(s): José Brant De Campos¹
¹ Rio de Janeiro State University

PPG-EM Seminars: season 2021
<http://www.ppgem.uerj.br>

Dec 17, 2021

Keywords: Graohene, Nanocomposite, Guarded Hot Plate, Thermal Conductivity.

1 Introduction

In nanocomposites, the distance among the particles changes the thermal conductivity of the material. The addition of nanoparticles increases thermal conductivity as the distance between the nanoparticles in the matrix decreases.[3]

2 Materials and Methods

This work aims to investigate the thermal properties of a polymeric nanocomposite reinforced with graphene oxide (GO) nanoparticles using instrumented equipment for measuring thermal conductivity. Measurements will be performed by the standard Guarded Hot Plate method.

2.1 Specimen

The materials used for the specimen were oxidized graphene and polyurethane. In this work, we use ultrasonic Tip to increase the dispersion of graphene oxide on polyurethane compared to using only magnetic stirrer. Table 1 provides information on the specimen used for the test.[2]

SPECIMEN	COMPOSITION	METHOD
1	Polyurethane	
2	0,50% GO	Ultrasonic Tip
3	0,50% GO	Magnetic Stirrer

Table 1: Specimens used for the tests

2.2 Guarded Hot Plate

In this method the test specimen is sandwiched between a hot and a cold plate. The hot plate has an electric resistance that dissipates heat through Joule effect. All hot plate faces are thermally insulated through temperature equality provided by internal hot water circulation with a closed loop control unit, except the face in con-

tact with the specimen, to where all heat flux is driven. The cold plate has a similar internal water circulation for continuous heat removal as shown in Figure 1.[4]

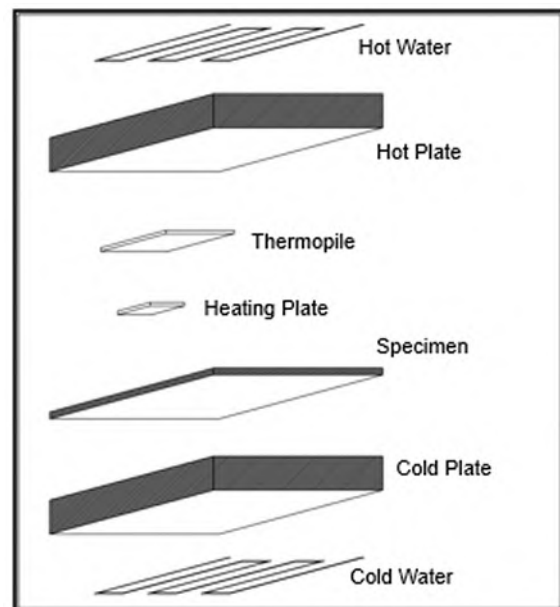


Figure 1: Guarded-Hot-Plate Method Set Up

2.3 Equipment

The equipment is formed by four main sections: fixed lower plate (cooling plate), movable upper plate (heating plate), protective sheet and measuring devices. The measuring devices consists of thermometers, rotometer, ammeter, voltmeter and micrometer that measure (0.001 mm) in thickness of the specimen. The hot plate is heated by electricity it has dimensions 250x250 mm and can measure up to 70mm sample thickness and the cold plate is cooled by water it has dimensions 250x250 mm like hot plate . The degree of heating and cooling can be adjustable by electricity and flow water control. The heat from the hot and cold plates is controlled by thermometers[1] . The coolant water must be at 15 C for the equipment working. Due to the hot climate in Rio de Janeiro, it was necessary

to add reservoir, pump and a refrigerator set in a closed circuit, as shown in Figure 2.

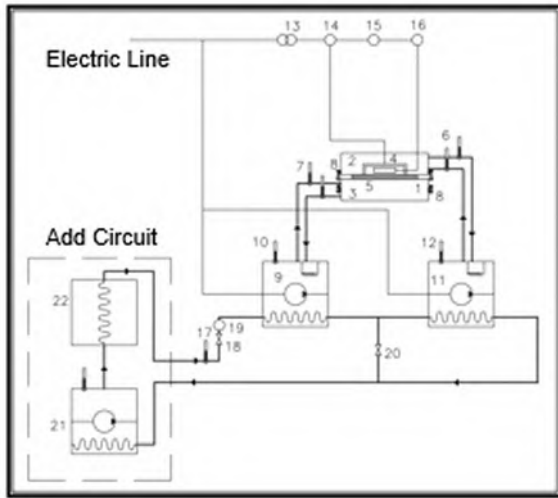


Figure 2: Closed Circuit adaoted for Rio de Janeiro

1. Specimen
2. Hot plate
3. Cool plate
4. Guard hot plate
5. Thermopile
6. Hot water inlet and outlet thermometers
7. Cold water inlet and outlet thermometers
8. Thickness measuring micrometers
9. Calorimeter
10. Heat regulator for 9
11. Calorimeter
12. Heat regulator for 11
13. Variable transformator
14. Two point adjuster
15. Ammeter
16. Voltmeter
17. Cool water thermometer
18. Cool water valve
19. Flow meter
20. Short circulation valve
21. Calorimeter
22. Refrigerator

2.4 Heat Conduction Determination

The heat flow is in steady-state and one-dimensional. To determine the heat conductivity we must use the Fourier's law.[4]

$$Q = V \cdot I \quad (1)$$

$$\lambda = \frac{Q \cdot e}{A \cdot \Delta T} \quad (2)$$

Q	Heat flo
V	Voltage
I	Corrent
e	Thickness of the specimen
A	Area of the specimen
ΔT	Temperature diference through the specimen
λ	Conductivuty

Table 2: Variables

3 Expected Results

Through the test on the equipment, it is expected from the experimental measurements that the thermal conductivity of the nanocomposite formed by polyurethane with oxidized graphene nanoparticles is greater than the thermal conductivity of the polyurethane without nanoparticles.

References

- [1] Mila R. Avelino, Manoel A. F. Consta Filho, and Roberto de Souza. Desenvolvimento de material didático para ensino de transferência de calor. Technical report, UERJ, 1999.
- [2] Alesandro Eronides de Lima Silva. Influencia da dispersão go e rgo em nanocompositos de poliuretano em aplicações de membranas para permeação de gases em recobrimento do aço api 5l x80. Master's thesis, UERJ, Oct 2019.
- [3] Roberto de Souza. *Graphene. Fundamentals and emergent applications*. Elsevier, 2013.
- [4] ASTM Designation. *Standard Test Method for Steady-State Heat Flux Measurements and Thermal Transmission Properties by Means of the Guarded-Hot-Plate Apparatus*. 2019.

